exceeds that of the reference beam (P_{ref}). The switching threshold can thus be controlled by the reference beam. The LED driver is current-balanced: if the LED is off, the current flows through MESFET M1, and the LED is turned on by pinching off M1.

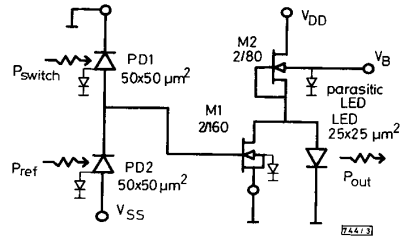

Fig. 3 *Schematic diagram of threshold circuit including parasitic LEDs connected to MESFETs and PDs*

The dimensions of the MESFET gates in the diagram are given by length/width

The output power is 30μW in the ON state, and a contrast ratio greater than 1000 has been estimated (Fig. 4). The minimum switching power is measured to be 3nW at vanishing reference power. At a differential input power of 50nW between P_{ref} and P_{switch}, the circuit has a switching delay of 43μs, which corresponds to a switching energy of 2 pJ. The photodetector area is twice 50 × 50μm² and the whole circuit, consisting of two PDs, two MESFETs and an LED, occupies 200 × 200μm². The power dissipation remains constant at 15mW.

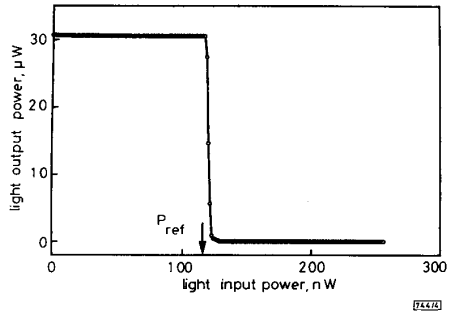

Fig. 4 *Switching behaviour of threshold circuit*

P_{ref} = 118nW, V_{DD} = 4V, V_{SS} = 2–V, V_B = 1.5V

Conclusion: We have developed a layer structure grown in a single step and a fabrication process for the monolithic integration of cascadable optoelectronic smart pixels. A threshold circuit with low switching power and switching energy has been demonstrated. The performance of such circuits is suitable for application in the fields of parallel optical interconnects and optoelectronic neural networks.

Acknowledgments: The authors respectfully acknowledge the discussions with J.E. Epler, K.H. Gulden and M. Moser and for the support of W. Bächtold, W. Kündig and J. Mlynek.

23 September 1994
Electronics Letters Online No: 19941380

U. Kehrli, D. Leipold, K. Thelen, H.P. Schweizer, P. Seitz and B. D. Patterson (*Paul Scherrer Institute, Badenerstr 569, Ch-8048 Zurich, Switzerland*)

References

1 BROWN, J.J., GARDNER, J.T., and FORREST, S.R.: 'An integrated, optically powered, optoelectronic 'smart' logic pixel for interconnection and computing applications', *IEEE J. Quantum Electron.*, 1993, **QE-29**, pp. 715–726

2 WOODWARD, T.K., LENTINE, A.L., CHIROVSKY, L.M.F., and ASARO, L.A.D.: 'GaAs/AlGaAs FET-SEED receiver/transmitters'. OSA Proc. Photonics in Switching, 1994, Vol. 16

3 EGAWA, T., JIMBO, T., and UMENO, M.: 'Monolithic integration of AlGaAs/GaAs MQW laser diode and GaAs MESFET grown on Si using selective regrowth', *IEEE Photonics Technol. Lett.*, 1992, **4**, pp. 612–614

4 CHENG, J., ZHOU, P., SUN, S.Z., HERSEE, S., MYERS, D.R., ZOLPER, J., and VAWTER, G.A.: 'Surface-emitting laser-based smart pixels for two-dimensional optical logic and reconfigurable optical interconnections', *IEEE J. Quantum Electron.*, 1993, **QE-29**, pp. 741–756

5 SHIH, Y.-C., MURAKAMI, M., WILKIE, E.L., and CALLEGARI, A.C.: 'Effects of interfacial microstructure on the uniformity and thermal stability of AuNiGe ohmic contact to *n*-type GaAs', *J. Appl. Phys.*, 1987, **62**, pp. 582–590

6 DESALVO, G.C., TSENG, W.F., and COMAS, J.: 'Etch rates and selectivities of citric acid/hydrogen peroxide on GaAs, $Al_{0.3}Ga_{0.7}As$, $In_{0.2}Ga_{0.8}As$, $In_{0.52}Ga_{0.48}As$, and InP', *J. Electrochem. Soc.*, 1992, **139**, (3), pp. 831–835

Noise and small-signal performance of three different monolithic InP-based 10Gbit/s photoreceiver OEICs

D. Kaiser, F. Besca, H. Großkopf, I. Gyuro, J.-H. Reemtsma and W. Kuebart

Indexing terms: Integrated optoelectronics, Optical receivers, Semiconductor device noise

Three circuit concepts (high impedance, common gate, and transimpedance) for a 10Gbit/s monolithic receiver OEIC consisting of an InGaAs/InP *pin* photodiode and InAlAs/InGaAs/InP HEMTs are compared in terms of noise and small-signal performance using on-wafer measurements. A total equivalent input noise current of 13.5pA/√Hz within the bandwidth of the transimpedance circuit is the lowest value ever reported for a monolithic InP-based 10Gbit/s receiver OEIC.

For long-haul lightwave communication systems there is an increasing interest in 10Gbit/s components. However, it has not been clear to date which concept will be successful in providing a high-performance but low-cost optical receiver. Monolithically integrated receiver front ends offer lower parasitics than hybrid solutions, which is essential for obtaining the highest bit rates. However, obviously the noise of the integrated devices is still too high. Today the best monolithic result reported is a 7.4GHz bandwidth circuit with a sensitivity of –17.3dBm at a bit error ratio of 10^{-9} for a 10Gbit/s NRZ signal [1]. The sensitivity was traced back to a total medium input noise current of 25 pA/√Hz. We present on-wafer measurements on three different circuit concepts for an InP-based monolithic photoreceiver using an InGaAs/InP *pin* photodiode and InAlAs/InGaAs/InP HEMTs. The circuits with increasing complexity, from a simple high impedance OEIC over a common gate circuit with source follower up to a transimpedance-cascode circuit, are shown in Fig. 1 and are compared in terms of bandwidth, responsivity, electrical output matching, and noise current.

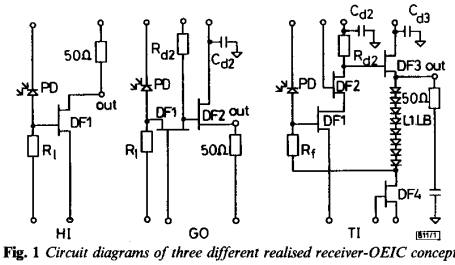

Fig. 1 *Circuit diagrams of three different realised receiver-OEIC concepts*

The integration concept, which is described elsewhere [2], is based on process technologies which take into account the aspect of possible future fabrication: low pressure metal organic vapour phase epitaxy, diffusion, and optical lithography. The 45μm diameter *pin* photodiedes have an optical window of 30μm, the responsivity observed at 1300nm is 0.85A/W, and the dark current is of the order of 10 nA at a reverse bias voltage of 5V. The HEMTs (1 × 100μm² gate area) exhibit a gate leakage current of ~5μA at maximum transconductance (330mS/mm); the extrinsic transit frequency is around 35GHz. Resistors are realised using the HEMT layers. The capacitance of the MIM capacitors is ~7pF with an isolation resistance of typically better than 500kΩ. The series resistance of the level shifter diodes at a forward bias of 10 – 20mA is ~6Ω.

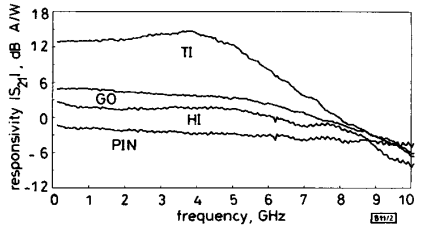

Fig. 2 *Transfer functions of three monolithic OEICs and one discrete pin photodiode*

The high-frequency characteristics of these optoelectronic circuits are measured using the on-wafer probing technique and a network analyser to modulate the 1300nm calibrated laser source of a lightwave testset. A lightwave probe with a singlemode lensed fibre is used to illuminate the *pin* photodiodes of the OEICs whereas a coplanar probe tip is used to detect the electrical response on-wafer. To provide the diverse DC biases to the circuits, coplanar multiple-power probe tips are used. In Fig. 2 the de-embedded (see [3]) optoelectronic transfer functions, i.e. the high frequency responsivity $|S_{21}|$ of the three different types of OEICs and, in addition, of one discrete *pin* photodiode, are shown in the frequency range 0 – 10GHz. The responsivity is calibrated in A/W. The lowest trace (named pin) belongs to the *pin* photodiode and was measured at a reverse bias voltage of 5V. A 3dB bandwidth of the order of 10GHz can be observed. From the lowest measured modulation frequency (130Hz) a responsivity of –1.3dB A/W (0.86 A/W) is determined. The other traces are transfer functions of three different types of OEIC. The high impedance circuit called HI reveals a fairly low responsivity of 2.8dB A/W (1.38A/W) due to the value R_l = 60Ω of the load resistor, which is necessary to achieve the observed bandwidth of 6.1GHz. The small-signal response of the common gate-circuit GO with source follower can also be seen in Fig. 2. The trace is very smooth without any reflective effects and reveals a 3dB bandwidth of 6.8GHz. The responsivity of 5dB A/W (1.78A/W) is somewhat higher compared to the high impedance OEIC. The transimpedance-cascode circuit TI uses a feedback resistor of approximately R_f = 300Ω and operates stably in the whole frequency range. As can be seen in Fig. 2 it attains the highest responsivity of 12.9dB A/W (4.41A/W). Taking into account the responsivity of the *pin* photodiode (–1.3dB A/W) a gain of 14.2dB is determined for the transimpedance circuit in the 50Ω system. This means that the transimpedance of the electrical part of the OEIC is ~260Ω. The trace shows a 3dB bandwidth of more than 5.5GHz and no excessive peaking.

The magnitude of the electrical output reflection $|S_{22}|$ of all three OEICs of Fig. 2 in the same operating point is depicted in Fig. 3 again in the frequency range of 0 – 10GHz. As can be observed, the high impedance circuit HI is highly reflective showing values in the order of only –1dB for the magnitude of the output reflection. The transimpedance circuit TI is somewhat better matched, starting at low frequencies at –3dB. When the transimpedance circuit exceeds the 3dB bandwidth the matching improves, but in the vicinity of the bandwidth a slight increase in the output reflection is observed. In contrast, the common-gate circuit GO using a source follower achieves a very good matching to the 50Ω measurement system of better than –12dB in the whole frequency range. This is the explanation for the very smooth transfer function without reflective effects observed for the GO circuit in Fig. 2.

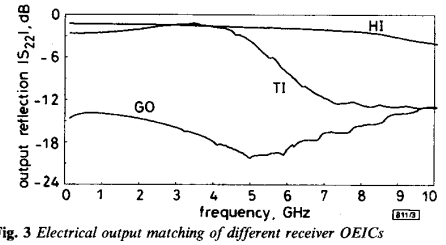

Fig. 3 *Electrical output matching of different receiver OEICs*

The noise properties of the circuits are also investigated on-wafer. Without any optical input signal the output noise current is measured using a broadband low-noise amplifier (as the second amplification stage) and a spectrum analyser. The equivalent input noise current density is calculated using the gain of the OEIC as the device under test (gain 1: see Fig. 2) as well as the main amplifier (gain 2 ≃ 34.5dB, noise figure *NF*2 ≃ 2dB). In Fig. 4 the equivalent input noise current density of all three types of OEIC of Fig. 2 is shown in the frequency band of interest, i.e. the bandwidth of the devices. It is obvious, that the transimpedance-cascode circuit TI reveals the lowest equivalent input noise current density whereas the high impedance circuit HI with a load resistance of only R_l = 60Ω shows the highest noise. On the other hand, the gate circuit with source follower GO is a good compromise between noise performance and circuit complexity. Again, the trace of the common-gate circuit GO is clearly smoother than all other traces due to the good output matching of the source follower. The total medium noise currents of all three OEICs (HI, GO, and TI) from 0.1 – 5.1GHz are 31, 20 and 13.5pA/√Hz, respectively. The transimpedance circuit shows values down to 11pA/√Hz in the frequency range 1 – 2GHz.

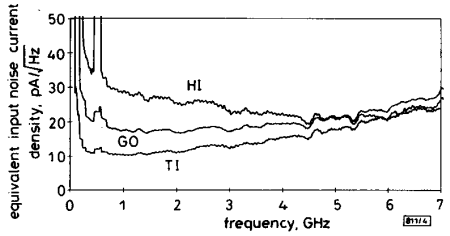

Fig. 4 *Equivalent input noise current density of different OEICs*

In conclusion, the on-wafer comparison of three different circuit concepts of InP-based monolithic receiver OEICs consisting of InGaAs/InP *pin* photodiodes and InAlAs/InGaAs/InP HEMTs has been performed. For 10Gbit/s operation the small-signal measurements show a sufficient bandwidth of more than 5GHz for all circuits, high impedance, common gate, and transimpedance circuit, but significant differences in responsivity or gain and electrical output matching. On-wafer noise current measurements reveal a total input noise current of 13.5 pA/√Hz for the transimpedance circuit, which is the lowest value reported so far for a monolithic InP-based 10Gbit/s receiver OEIC.

Acknowledgments: The excellent support of our colleagues H. Conrad, H. Groß, F. Grotjahn, G. Luz, and G. Müller is gratefully acknowledged. This work was partially financed by Deutsche Bundespost Telekom.

30 September 1994

Electronics Letters Online No: 19941397

D. Kaiser, F. Besca, H. Großkopf, I. Gyuro, J.-H. Reemtsma and W. Kuebart (*Alcatel SEL Research Centre, Dep. Opto-Electronic Components ZFZ/WO, Lorenzstr. 10, D-70435 Stuttgart, Germany*)

References

1 AKATSU, Y., MIYAGAWA, Y., MIYAMOTO, Y., KOBAYASHI, Y., and AKAHORI, Y.: 'A 10Gb/s high sensitivity, monolithically integrated p-i-n-HEMT optical receiver', *IEEE Photonics Technol. Lett.*, 1993, **5**, pp. 163–165

2 KUEBART, W., REEMTSMA, J.-H., GROßKOPF, H., GYURO, I., KAISER, D., CONRAD, H., GROSS, H., GROTJAHN, F., and EISELE, H.: 'Monolithically integrated 10Gb/s InP-based receiver OEIEs: Design and realization'. Conf. Proc. 19th ECOC, 1993, (Montreux, Switzerland), pp. 305–308

3 KAISER, D., GROßKOPF, H., GROTJAHN, F., GYURO, I., KUEBART, W., REEMTSMA, J.-H., and EISELE, H.: 'De-embedding of on-wafer lightwave measurements performed on a monolithic 10Gb/s InP reveiver-OEIC'. Proc. 23rd European Microwave Conf., 1993, (Madrid, Spain), Paper B 6.1, pp. 361–363

Extraction of natural frequencies of radar target by L^2 space optimisation

J. Li and L. Jen

Indexing terms: Radar cross-sections, Target identification

A new method (L^2M) for extracting the natural frequencies of a radar target is presented. The method is based on L^2 space optimisation. The superiority of this method to the tradional L^2 space optimisation method (l^2M) in the presence of random noise is analysed and demonstrated by simulation computations.

Introduction: Because the natural frequencies of any scatterer have a unique distribution in the complex plane, they can be used for target identification and discrimination. As the extraction of the natural frequencies of scatterers is an inevitable step in practical applications, it becomes necessary to develop a method, which should be as insensitive to random noise as possible, for extracting the natural frequencies from a measured response of the scatterer.

Although the conventional nonlinear scheme [1] is somewhat less sensitive to random noise than some other methods, such as the Prony method [2], it still cannot meet practical requirements. In this Letter a new scheme is proposed.

New method: It is assumed that the late time response of a radar target obeys the natural mode representation

$$F(X,t) = 2\sum_{i=1}^{2M}(c_i\cos(w_i t) + d_i\sin(w_i t))e^{a_i t} \quad t > t_L \quad (1)$$

where $S_i = a_i + jw_i$ and $R_i = c_i + jd_i$ are, respectively, the natural frequency and the residues of the ith mode, and $X = (c_1, \ldots, c_m, d_1, \ldots, d_m, a_1, a_m, w_1, \ldots, w_m)^T$ is the vector containing the unknown natural frequencies and residues.

To obtain a better estimate of S_i and R_i, instead of minimising

$$I(X) = \sum_K [F(X,t_k) - r_k]^2 \quad (2)$$

as is done in [1], where $r_k = r(t_k)$ are the sampled late time target response, and $F(X, t)$ is the fitting function given by eqn. 1, we minimise

$$L(X) = \int [F(X,t) - R(t)]^2 dt \quad (3)$$

where $F(X, t)$ is also the fitting function given by eqn. 1, and $R(t)$ is the linear interpolating function of the sampled target response. Here $F(X, t)$ and $R(t)$ are both vectors in L^2 space.

Solving the problem $L(X) = 0$ by the Newton method requires a good initial guess for convergence. We also employ the continuation method to overcome this difficulty as done in [1]. That is, we minimise

$$H_R = p\int [F(X,t) - R(t)]^2 dt + (1-p)\|X - X_0\| \quad (4)$$

where X_o is an initial guess, and solve the series of problems $p = 0$, $p_1, p_a, \ldots, 1$.

Because the integration in eqn. 3 can be carried out analytically prior to the minimising procedure, the new method can save much computing time.

Discussion of method: The reasons for the success of the new method in the presence of random noise can be identified by investigating the difference between the l^2M method and L^2M method. The l^2M method finds out the unknown vector X from eqn. 2 using the following iteration process:

$$\begin{cases} (DF^T \cdot DF) \cdot P = DF^T \cdot F - DF \cdot R \\ X_{k+1} = X_k - \omega \cdot P_k \end{cases} \quad (5)$$

where $R = (r_1, r_2, \ldots, r_N)^T$ is a vector formed by the measured data. $F = [F(X, t_1), F(X, t_2), \ldots, F(X, t_N)]^T$. The superscript T denotes the transpose of a matrix, and

$$DF = \begin{bmatrix} \dfrac{\partial F(X,t_1)}{\partial x_1}, \ldots, \dfrac{\partial F(X,t_N)}{\partial x_1} \\ \dfrac{\partial F(X,t_1)}{\partial x_2}, \ldots, \dfrac{\partial F(X,t_N)}{\partial x_2} \\ \dfrac{\partial F(X,t_1)}{\partial x_N}, \ldots, \dfrac{\partial F(X,t_N)}{\partial x_N} \end{bmatrix}$$

The L^2M method determines the unknown vector X from eqn. 3 using the following iteration process:

$$\begin{cases} \left\langle \dfrac{\partial F(X,t)}{\partial x_i}, \dfrac{\partial F(X,t)}{\partial x_j} \right\rangle P_k = \left\langle \dfrac{\partial F(X,t)}{\partial x_i}, F(X,t) \right\rangle \\ \qquad\qquad - \left\langle \dfrac{\partial F(X,t)}{\partial x_i}, R(t) \right\rangle \\ X_{k+1} = X_k - \omega \cdot P_k \end{cases} \quad (6)$$

where $F(X, t)$ is the fitting function given by eqn. 1, and

$$R(t) = \begin{cases} r_i + (r_{i+1} - r_i)(t - t_i)/DT & t_{i+1} > t > t_i \\ 0 & \text{otherwise} \end{cases}$$

The brackets $\langle \cdot\ , \cdot \rangle$ indicate the inner product

$$\langle f(t), g(t) \rangle = \int f(t) \cdot g(t) dt$$

Comparing the processes of eqns. 5 and 6, it can be easily seen that:

(i) The l^2M method has to perform many multiplications and summations to obtain each element of the matrix $(DF^T \cdot DF)$ and each element of the vector $(DF^T \cdot DF)$ in eqn. 5, and such operations are iterated many times. Hence computational errors are produced. As the extraction of the natural frequencies is an ill-conditioned problem [1], the computational errors will lead to serious errors in the final results.

The L^2M method can compute each element of the matrix $[\partial F(X, t)/\partial x_i, \partial F(X, t)/\partial x_j)]$ and each element of the vector $[\partial F(X, t)/\partial x_j, F(X, t)]$ in eqn. 6 analytically, without introducing numerical errors. The final computed results are much more accurate than those of the l^2M method.

(ii) The l^2M method uses discrete values r_i of the measured response to obtain the entries of the vector $(DF^T \cdot R)$ in eqn. 5.

The L^2M method computes the entries of the vector $[\partial F(X, t)/\partial x_i, R(t)]$ in eqn. 6 first by interpolating linearly between the sample points, and then integrating the product analytically, both interpolating and integration performing a smoothing of the measured data.

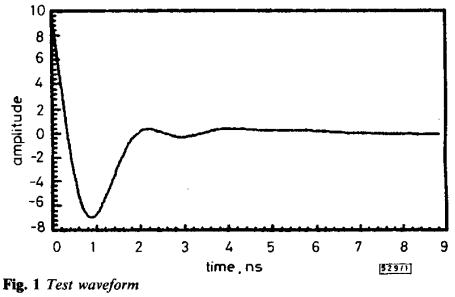

Fig. 1 *Test waveform*

Example: An arbitrary case is used to show the superiority of the L^2M method to the l^2M method. Consider the case $n = 5$ ($N = 10$)